NJC

ROYAL SOCIETY OF CHEMISTRY

PAPER

View Article Online
View Journal | View Issue

Cite this: *New J. Chem.*, 2023, **47**, 4052

Synthesis and properties of hollow Fe_3O_4@Au hybrid nano-structures for T_1–T_2 MR imaging and a combination of magnetic and photo-induced heating†

Nguyen T. N. Linh,[a] Ngo T. Dung,*[b] Le T. T. Tam,[b] Le T. Tam,[c] Nguyen P. Hung,[a] Nguyen D. Vinh,[a] Ngo T. Ha,[a] Pham. H. Nam,[e] Le V. Thanh,[f] Nguyen V. Dong,[f] Le G. Nam,[f] Nguyen V. Dang,[a] Nguyen X. Phuc,[e] Le D. Tung,[gh] Nguyen T. K. Thanh[gh] and Le T. Lu*[bd]

Received 4th October 2022,
Accepted 16th January 2023

DOI: 10.1039/d2nj04880a

rsc.li/njc

In the current work, hollow Fe_3O_4@Au hybrid nanoparticles (h-NPs) with a size of 17 nm were synthesised through seeded growth and galvanic replacement reactions. The influence of the experimental parameters such as the reaction time and precursor concentration on the formation of h-NPs was investigated. The hydrophobic hollow Fe_3O_4@Au h-NPs were transferred into water by coating with an amphiphilic polymer, poly(maleic anhydride-*alt*-1-octadecene) (PMAO), to form highly stable colloids. The PMAO coated hollow Fe_3O_4@Au h-NPs provide an excellent signal enhancement of T_1- and T_2-weighted MRI (r_1 = 8.47 mM^{-1} s^{-1}, r_2 = 74.45 mM^{-1} s^{-1}). Magnetic and photothermal data of the hollow Fe_3O_4@Au h-NPs indicated that sample temperature can reach 70 °C under a magnetic field of 16 kA m^{-1} and a frequency of 450 kHz for 2 min and 808 nm NIR laser at a power density of 0.65 W cm^{-2} for 2 min. This effective combination between the magnetic thermia of the magnetic cores and the photothermal effect of the gold shell indicates hollow Fe_3O_4@Au h-NPs as a potential material for efficient cancer theranostics.

Introduction

In recent years, multifunctional h-NPs, which have several properties of discrete NPs integrated into hybrid nanostructures,[1–4] have attracted special attention due to their potential applications such as in biomedicine,[3,5–12] electronic,[13] catalysis,[14–16] and wastewater treatment.[17,18] For example, the magneto-plasmonic core–shell nanostructures can be used for applications of antimicrobials,[19–21] imaging diagnostics,[19] magnetic hyperthermia,[22,23] optical hyper-thermia,[24] and magneto-photothermal therapy.[25–27] This is due to the magnetic nature of the core along with optical properties of the plasmonic shell in a single nanosystem.

Currently, the utilisation of magnetic-plasmonic h-NPs for biomedical purposes focuses mainly on Fe_3O_4/Au h-NPs with core–shell, core–satellite, dumbbell-like or flower-like nanostructures. These h-NPs are synthesised with a seeded-growth method using Au NPs or Fe_3O_4 NPs as seeds.[13,28–32]

Thus far, the works on Fe_3O_4@Au h-NPs for imaging diagnostic and hyperthermia applications have obtained some remarkable results.[26,33,34] However, Fe_3O_4@Au h-NPs with an Au layer coated on the surface of the Fe_3O_4 core are usually solid nanostructures, which significantly limit the interaction of protons in the surrounding environment with the inside magnetic cores leading to the reduction of the T_2-weighted signal in the MRI application. Furthermore, these solid Fe_3O_4@Au h-NPs normally exhibit the surface plasmon resonance (SPR) peak positions in the range from 510 to 600 nm.[26,35] They are, therefore, less useful for *in vivo* applications, such as cancer cell imaging and photo-thermal therapy, where near-infrared light in the range of 650–900 nm is preferred due to its deeper

[a] *Thai Nguyen University of Sciences, Tan Thinh Ward, Thai Nguyen City, Thai Nguyen, Vietnam*
[b] *Institute for Tropical Technology, Vietnam Academy of Science and Technology (VAST), 18 Hoang Quoc Viet, Hanoi, Vietnam*
[c] *Vinh University, 182 Le Duan Street, Vinh City, Nghe An, Vietnam*
[d] *Graduate University of Science and Technology, VAST, 18 Hoang Quoc Viet, Hanoi, Vietnam*
[e] *Institute of Materials Science, VAST, 18 Hoang Quoc Viet, Hanoi, Vietnam*
[f] *Vinh International Hospital, 99 Pham Dinh Toai Street, Vinh City, Nghe An, Vietnam*
[g] *Biophysics Group, Department of Physics and Astronomy, University College London, Gower Street, London WC1E 6BT, UK*
[h] *UCL Healthcare Biomagnetics and Nanomaterials Laboratories, University College London, 21 Albemarle Street, London W1S 4BS, UK*

† Electronic supplementary information (ESI) available. See DOI: https://doi.org/10.1039/d2nj04880a

penetration into the body. Moreover, the synthesis of the solid Fe_3O_4@Au h-NPs (core–shell, dumbell-like nanostructures) includes large amounts of Au precursors being used, usually 8 times more than that of Fe_3O_4 NPs, and thus leading to a very high cost.[36]

Recently, to address the aforementioned issues, some Fe_3O_4–Au h-NPs with hollow nanostructures were developed. For example, X. Gao *et al.* reported on the synthesis of magnetic–gold core@shell h-NPs by creating a polymer gap between the magnetic core and the gold shell.[37] C. Xiaoyuan and co-workers reported on the yolk–shell Fe_3O_4@Au h-NPs with a gap between the Fe_3O_4 core and the porous Au layer.[38] Here, a relatively thick SiO_2 shell was applied on the magnetic core before coating gold. The SiO_2 layer was then chemically removed leaving hollow h-NPs. Y. Yadong *et al.* proposed a general approach for the synthesis of Fe_3O_4–M (M = Ag, Pt, and Au) h-NPs. The hollow Fe_3O_4–Au dumbbell-like h-NPs were obtained through a galvanic replacement reaction between Ag NPs in the h-NPs and gold ions.[39] The hollow h-NPs showed strong SPR absorption in the NIR region from 650 to 900 nm[40] but the particle size is relatively large (from 40 to 100 nm) significantly affecting the colloidal stability.

In this paper, we report the synthesis of hollow Fe_3O_4@Au h-NPs through galvanic replacement reactions between the Au precursor and Fe_3O_4@Ag h-NPs as nanotemplates. The as-synthesised hollow h-NPs have a small perimeter size of 17 nm with a gap between the Fe_3O_4 core and the Au shell and exhibit strong SPR absorption at around 700 nm. The as-synthesised hollow Fe_3O_4@Au h-NPs are encapsulated by PMAO to make them colloidally stable in water and biocompatible. The PMAO coated hollow Fe_3O_4@Au h-NPs were studied as agents for T_1–T_2 MRI, and for magnetic inductive heating (MIH) and the photothermal heating (PTH) modes.

Experimental

Chemicals

All chemicals, including precursors: iron(III) acetylacetonate ($Fe(acac)_3$, 99.9%), silver nitrate (99.8%), and gold(III) chloride hydrate ($HAuCl_4{\cdot}xH_2O$, 99.99%); surfactants and reductants: oleic acid (OA, 99%), oleylamine (OLA, 70%), 1-octadecanol (OCD-ol, 99%), and poly(maleic anhydride-*alt*-1-octadecene) (PMAO); and solvents: 1-octadecene (ODE, 90%), dibenzyl ether (99%), chloroform (99%), absolute ethanol (100%) and *n*-hexane (98.5%) were purchased from Sigma-Aldrich Ltd, Singapore. All the chemicals were used as received without further purification.

Gastric adenocarcinoma cell lines MKN-45 and AGS were ordered from RIKEN, BRC Cell Engineering Division, Japan; Gibco RPMI 1640 Medium, fetal bovine serum and vancomycin received from Invitrogen, Cergy-Pontoise, France and used for cell culture; DAPI (4′,6-diamidino-2-phenylindole) and MTT reagent (3-(4,5-dimethylthiazol-2-yl)-2,5-diphenyltetrazolium bromide) were purchased from Thermo Fisher, USA as the staining reagent chemicals. Dotarem®, a paramagnetic ionic MRI contrast agent, containing 0.5 mmol mL^{-1} gadoteric acid was obtained from Guerbet LLC, USA.

Synthesis of Fe_3O_4 NPs

Fe_3O_4 NPs were synthesised by thermal decomposition in organic solvents following our previous work.[41] In a typical synthesis, a mixture of $Fe(acac)_3$ (190 mM), OA (744 mM), OLA (744 mM), and OCD-ol (300 mM) were mixed in a 100 mL three-neck flask containing 40 mL of ODE under a nitrogen flow. The reaction mixture was magnetically stirred at room temperature for 30 min for de-gassing. The mixture was gradually increased to 100 °C and maintained at this temperature for 30 min to remove water. Then, the reaction temperature was heated up to 200 °C, and refluxed for another 30 min. Finally, the reaction solution was raised to 295 °C at a steady rate of 5 °C min^{-1}. At this temperature, the samples were removed with the reaction time intervals of 10, 30, 60, and 120 min to evaluate the growth of the NPs. The resulting mixture was cooled to room temperature by removing the heat source. Synthesised NPs were purified by centrifugation for 10 min at 12 000 rpm (or by approaching a magnetic bar for large NPs) using ethanol and redispersed in *n*-hexane. The NPs were dried before carrying out the characterisations.

Synthesis of Fe_3O_4–Ag h-NPs

The Fe_3O_4–Ag h-NPs were synthesised using the seeded-growth method. In a typical experiment, a mixture of 5 mL *n*-hexane containing 0.1 g purified Fe_3O_4 NPs, 1 g silver nitrate in 6 mL OLA, and 0.3 g OCD-ol were mixed with 40 mL ODE in a 100 mL three-neck flask under a nitrogen flow. The reaction mixture was heated to 80 °C and kept at this temperature for 30 min to remove *n*-hexane, then allowed to reflux at 200 °C at a heating rate of 5 °C min^{-1} and maintained for 60 min before cooling down to room temperature. In this study, the effect of the molar ratio of Ag to Fe on the morphology, monodispersity and dimensions of Fe_3O_4–Ag h-NPs was investigated.

The as-synthesised Fe_3O_4–Ag h-NPs were purified from free Ag NPs and excess ligands before characterisation. In a typical purification, 1 mL of a solution of Fe_3O_4–Ag h-NPs was mixed with 1 mL of ethanol by sonication. The Fe_3O_4–Ag h-NPs were collected by a magnetic bar and the supernatants containing mostly excess ligands and free Ag NPs were discarded. The Fe_3O_4–Ag h-NPs were then redispersed in 1 mL *n*-hexane and precipitated by adding 1 mL of ethanol. The purification procedure was repeated 2 more times and the final product was redispersed in 1 mL *n*-hexane.

Synthesis of hollow Fe_3O_4@Au h-NPs

The purified Fe_3O_4–Ag h-NPs were used as the nano-templates for the formation of hollow Fe_3O_4@Au h-NPs. The synthesis of hollow Fe_3O_4@Au h-NPs followed our previous work.[42] In a typical synthesis, 1 mL solution of the purified core–shell Fe_3O_4@Ag sample was diluted into 20 mL dibenzyl ether and stored in a three-neck flask. The solution was magnetically stirred and then slowly heated to the desired temperature. To this mixture, a certain volume of the gold salt solution

made of 15 mg $HAuCl_4 \cdot xH_2O$ dissolved in 15 mL dibenzyl ether and 0.5 mL OLA was added. The mixture was stirred until its colour became stable. The product was washed similarly to that of the Fe_3O_4–Ag samples, then the excess saturated ammonia solution was added to eliminate AgCl.

Phase transfer of hollow Fe_3O_4@Au h-NPs into water

The phase transfer process of hydrophobic hollow Fe_3O_4@Au h-NPs into water was carried out following previous works.[42,43] Briefly, a stock solution of PMAO in $CHCl_3$ with a concentration of 10 mg mL^{-1} was prepared. To this solution, 10 mL of chloroform containing hollow Fe_3O_4@Au h-NPs was added. The mixture was magnetically stirred for 60 min and dried at room temperature. Then diluted NaOH solution (10 mL) was added and sonicated for at least 10 min. The solution was then centrifuged at 12 000 rpm to precipitate the h-NPs. After removing the supernatant, the residue h-NPs were redispersed in water. The purification procedure was repeated several times and the final product was redispersed in 10 mL water.

Material characteristics

The morphology of the synthesized particles was observed on a transmission electron microscope JEM 1010 (JEOL, Japan). The crystalline phases of the materials were analyzed using an X-ray diffractometer (SIEMENS D5005) with $\lambda_{Cu\ K\alpha}$ = 15 406 Å. A vibrating sample magnetometer (VSM) was employed to measure the magnetic properties of the materials at room temperature. Particle size distribution of the materials was monitored using a Dynamic Light Scattering (DLS) method on a Nanosizer S (Malvern, UK). The optical properties of samples were recorded on a spectrophotometer (Jasco V-670, Japan). The chemical composition of the materials was determined through energy dispersive X-ray spectroscopy (EDS) and the elemental mapping analysis obtained from a Jeol JSM-6510LV instrument. Thermogravimetric Analysis (TGA) measurement was performed on a TG209F1 (NETZSCH-Germany) instrument. Fourier Transform Infrared (FT-IR) measurement was carried out using Nicolet iS10 (Thermo Scientific – USA) equipment.

In vitro cytotoxicity study

MTT assay. The cytotoxic effect of hollow Fe_3O_4@Au h-NPs on AGS and MKN45 cells was evaluated using an MTT assay. The cells were seeded in triplicate for each experimental condition in a 96-well plate at a concentration of 5×10^3 cells cm^{-2}, (n = 5 for each experimental condition). Cells were treated with various concentrations of hollow Fe_3O_4@Au h-NPs prepared in deionised water (dH_2O). A control group received the same amounts of dH_2O alone. After 24 and 72 h of the treatment, culture medium was replaced with 100 μL of fresh media and 20 μL of MTT reagent (5 mg mL^{-1}). Cells were continuously incubated in 5% CO_2 at 37 °C and 95% humidity for 4 h. Subsequently, the MTT solution was replaced by 100 μL dimethyl sulfoxide (DMSO) and 12 μL of Sorensen buffer (0.1 M NaCl, 0.1 M glycine adjusted to pH = 10.5 with 1 M NaOH) and incubated for 15 min at 37 °C. The optical density of the wells was measured at 570 nm using a spectrophotometric plate reader (Multiskan Sky Microplate Spectrophotometer, Thermo Fisher Scientific). Cell viability was determined using the formula: % cell viability = (optical density of sample/optical density of control) × 100%.

Cell and nuclear morphology. The effect of hollow Fe_3O_4@Au h-NPs on AGS and MKN45 cell morphology was monitored as follows: 2×10^6 cells were seeded in 24-well plates and treated with hollow Fe_3O_4@Au h-NPs at various concentrations for 72 h. Cellular imaging was performed using a phase-contrast light microscope (Eclipse Ts2, NIKON). Cellular nuclei were stained with DAPI at 1 : 5000 dilution of 10 mg mL^{-1}. After treatment with the h-NPs, the cells were washed twice with phosphate-buffered saline (PBS), permeabilised with 0.5% Triton X, 10 min and stained with the DNA-specific fluorochrome DAPI (Invitrogen). The cells were then washed with PBS and the fluorescence images of nuclear were observed using a NIKON Eclipse Ti2U fluorescence microscope (NIKON, Japan).

In vitro T_1 and T_2-weight MRI dual-modal imaging

The longitudinal and transverse relaxation times (T_1 and T_2) of the PMAO encapsulated hollow Fe_3O_4@Au h-NPs were measured on a 1.5 T MRI scanner, 64 MHz (Siemens Magnetom, Germany). The PMAO coated hollow Fe_3O_4@Au h-NPs were diluted to Fe concentrations in the range of 0.03 to 0.45 mM and placed in 2 mL vials. Longitudinal relaxation time T_1 was measured with a variable TR Turbo Spin-Echo sequence and the transverse relaxation time T_2 was measured with a fixed TR Spin-Echo sequence. Syngo@fastView, EFilm workstation (Merge Healthcare) and MatLab software were used to draw regions of interest (ROIs) and calculate the relaxation times. Decay curves were fitted with a mono-exponential decay equation to calculate T_2:

$$y = A + C \cdot e^{-TE/T_2} \quad (1)$$

and a mono-exponential growth saturation recovery equation to calculate T_1:

$$y = A + C(1 - e^{-TR/T_1}) \quad (2)$$

The longitudinal and transverse relaxation rates ($1/T_i$ or R_i, i = 1, 2) were plotted as a function of iron concentration, expressed in mM of iron, and the longitudinal and transverse (r_1, r_2) relaxivities were obtained by the slope of the fitting straight lines.

Decay curves were fitted with a mono-exponential decay equation to calculate T_2, where A is the absolute bias and C the signal intensity T_2 of the samples, which was measured using the Spin-Echo (SE) pulse sequence with the following parameters: effective TE, with 07 echoes ranging from 11 to 91 ms, TR = 4000 ms, 208×230 mm^2 x–y field of view (FOV), 4 mm slice thickness, and the number of averages of 2.

The T_1 value of the samples was measured using a Turbo Spin Echos (TSE) variable TR pulse sequence with the following parameters: TE = 11 ms, TRs ranging from 100–2500 ms, 200 mm × 200 mm x–y field of view (FOV), 4 mm slice

thickness, 192 × 320 matrix size providing 200 μm^2 x–y resolution, and the number of averages of 2.

Magnetic and photo induced heating

The MIH and/or PTH efficiencies of the hollow Fe_3O_4@Au h-NPs were carried out using a commercial generator UHF-20A (Chengdu JinKeZhi Electronic) providing an alternating magnetic field with a maximum amplitude of 16 kA m^{-1} and frequency of 450 kHz. The monochromatic laser 808 nm was supplied by Lasermate Group, Inc. The power density of the laser was measured on a Melles Griot 13PEM001 system of BMI Surplus, Inc. In every measurement, a 200 μL solution of hollow Fe_3O_4@Au h-NPs was used. The distance from the laser to the sample was 5 cm, the diameter of the laser spot was 2 mm, and the diameter of the sample tube was 3 mm. The temperature of the sample was monitored in-situ along with the irradiation using a platinum resistance thermometer (PT 100 sensor) and connected to a computer through the USB port. The evaluation of the conversion of absorbed energy of a magnetic field and/or light into heat (specific loss power, SLP) was experimentally determined using the following equation.[44]

$$\mathrm{SLP(W\,g^{-1})} = C\frac{m_s}{m_n}\frac{dT}{dt} \quad (3)$$

where m_s is the mass of the sample, m_n is the mass of the hollow Fe_3O_4@Au h-NPs in the nanofluid, C is the specific heat capacity of water (4.185 J g^{-1} K^{-1}) and dT/dt is the heating rate determined from the experimental curves.

Result and discussion

Fe_3O_4 magnetic NPs

Fe_3O_4 NPs were prepared by thermal decomposition of $Fe(acac)_3$ in ODE under the presence of OA/OLA (the volume ratio of OA : OLA = 1 : 1) as stabilising agents and OCD-ol as reducing/accelerating agents following our previous work.[41] The influence of synthetic conditions such as the concentration of reagents, temperature and reaction time on the formation of Fe_3O_4 NPs were investigated (Table S1, ESI†). Fig. 1 shows TEM images and the corresponding size distribution histograms of Fe_3O_4 NPs synthesised at different reaction durations. It can be seen that the obtained NPs are spherical and monodisperse. The particle size increases from 3.4 to 13.9 nm with the increase of the reaction time from 10 to 120 min. The longer the reaction time, the larger the NPs were obtained. This increasing trend of the particle size over a 2 h reaction period is similar to the synthesis of the ferrite NPs.[41,45]

In this study, the influences of the concentration of the surfactant and precursor on the evolution and monodispersity of Fe_3O_4 NPs were also investigated and the obtained results are shown in Table S1 and Fig. S1, S2 (ESI†). TEM images and particle size distribution histograms (Fig. S1 and S2, ESI†) indicate that spherical and monodisperse NPs with particle sizes in the range of 6.3–14.7 nm were obtained.

(a) Effect of precursor concentrations. The Fe_3O_4–Ag h-NPs were synthesised by reducing Ag^+ ions on the surfaces of Fe_3O_4 NPs in the presence of OLA and in ODE solvent (Experimental

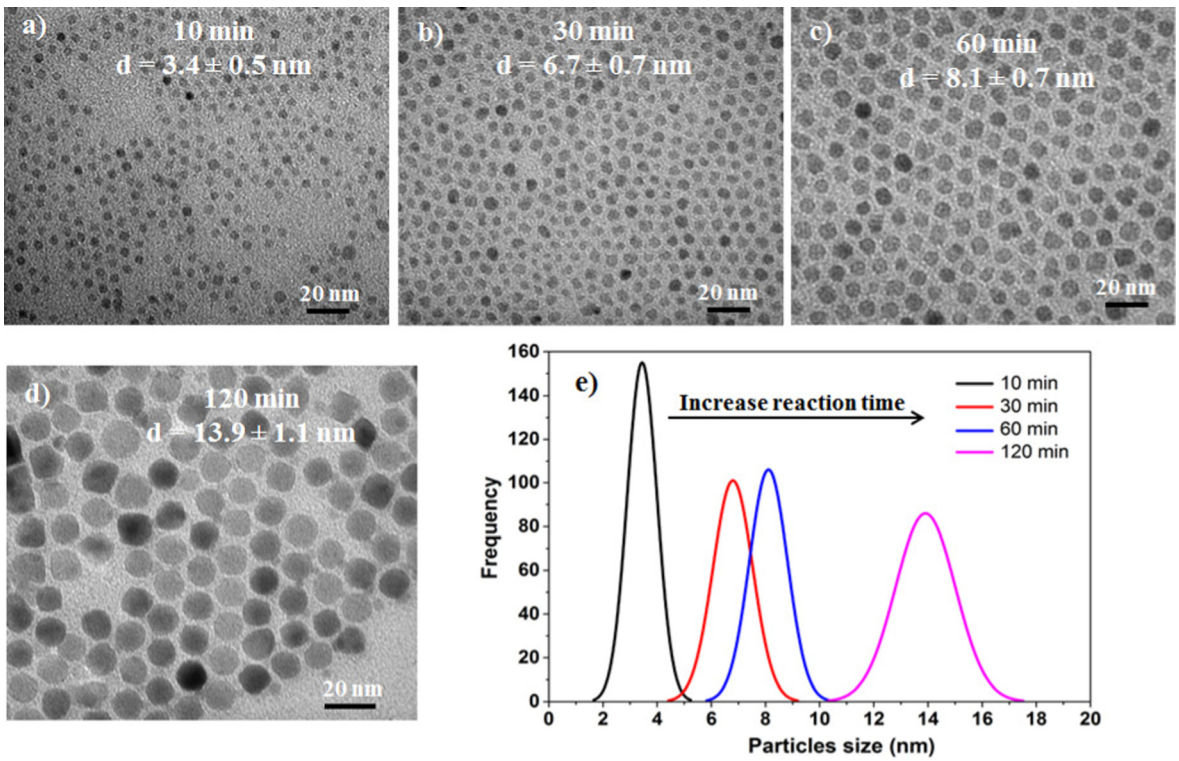

Fig. 1 TEM images of Fe_3O_4 NPs synthesised at different reaction times: (a) 10, (b) 30, (c) 60, and (d) 120 min; and the corresponding size distribution histograms (e). The concentration of the reagents: $Fe(acac)_3$ = 190 mM; OA = OLA = 744 mM.

Table 1 Influence of the reaction conditions on the morphology of Fe_3O_4–Ag h-NPs

ε = [Ag]/[Fe]	Reaction time (min)	Morphology of Fe_3O_4–Ag h-NPs
0.5, 1.4, 2.3, 3.2	30	Core–shell
	60	Core–shell
4.5, 6.8	30	Core–shell
	60	Core–shell
	120	Core–shell
9.0	30	Dumbbell-like and core–shell
	60	Dumbbell-like and core–shell
	120	Dumbbell-like and core–shell
11.4, 13.6	30	Dumbbell-like
	60	Dumbbell-like
	120	Dumbbell-like

section). Here, Fe_3O_4 NPs (8.1 ± 0.7 nm) were used as seeds for the growth of Fe_3O_4–Ag hybrid nanostructures. The influence of synthetic conditions on the morphology and monodispersity of the h-NPs was investigated. Table 1 summarises the influence of synthetic conditions including reaction time and the ratio of Ag to Fe concentration on the morphology of the h-NPs.

Fig. 2 shows the TEM images and size distribution histograms of Fe_3O_4–Ag h-NPs synthesised at different ratios of Ag to Fe concentration. Within the investigated Ag^+ concentration range, the morphology and monodispersity of the Fe_3O_4/Ag h-NPs depend on the molar ratio of Ag to Fe (ε = [Ag]/[Fe]). When ε varies from 0.5 to 6.8, we obtained Fe_3O_4–Ag h-NPs with a core–shell structure. While increasing the ε value to 9.0, a mixture of core–shell and dumbbell-like nanostructures was formed (Table 1).

The dependence of the morphology (size and shape) of the Fe_3O_4–Ag h-NPs on the precursor ratio was also reported by Grzybowski *et al.*[28] In addition, the transformation from core/shell to dumbbell-like structures was previously explained by Elena V. Shevchenko.[46] At a low silver salt concentration, a core/shell structure is formed. Due to the different crystal structures of the core and the shell materials, the formed hybrid nanostructure can have lattice mismatch and strain. The interface energy between the seed and the Ag shell increased by the distortion of the lattice. As the layer thickness of the core/shell structure increases due to raising of the precursor ratio, strain energy originating from the deformation increases. When the thickness of the Ag shell exceeds the critical value, the morphological change from core/shell to dumbbell takes place to reduce the contact area between the seed and the Ag domain.

At ε = 1.4, a mixture of the small and large spherical particles was observed (Fig. 2a). The small NPs were possibly uncoated Fe_3O_4 NPs (having the light contrast, due to the lower electron density compared to Ag) or the NPs coated with a very thin Ag shell and the large ones with an average diameter of 12.5 ± 1.9 nm likely core–shell Fe_3O_4@Ag h-NPs or Ag NPs. Nevertheless, the shell thickness was uneven which is due to the low content of $AgNO_3$ precursor. When the ε value increases to 3.2 and 6.8, the core–shell h-NPs were monodisperse with the

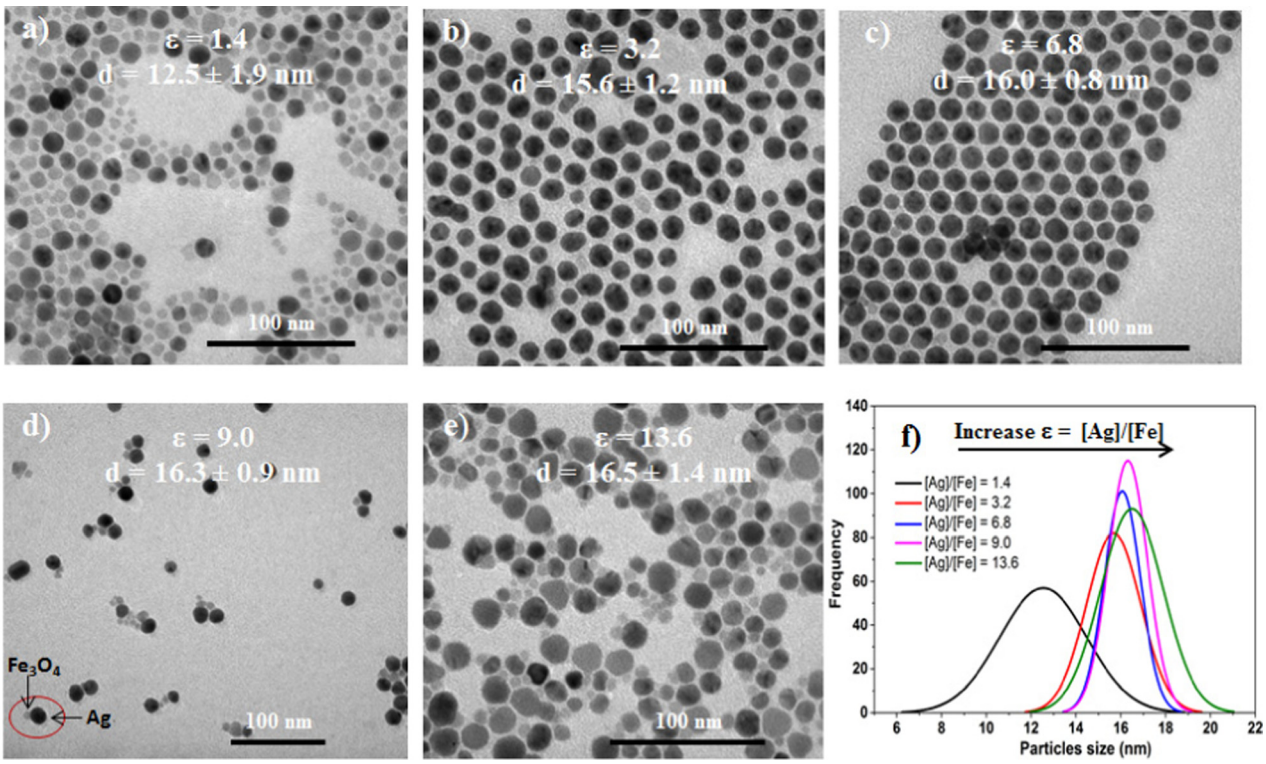

Fig. 2 TEM images of Fe_3O_4@Ag h-NPs and their histogram of particle size distribution synthesised at different values of ε = [Ag]/[Fe]. Fe_3O_4 NPs with particle sizes of 8.1 nm were used as seeds.

particle of around 16 nm. Free or uncoated Fe_3O_4 NPs are not observed on the TEM images (Fig. 2b and c).

At $\varepsilon = 9.0$, beside the core–shell h-NPs (about 20–25%), there are also dumbbell-like Fe_3O_4–Ag h-NPs consisting of a Fe_3O_4 NP attached to an Ag one (Fig. 2d). The small particles with a size of 8.1 ± 0.7 nm (grey) are magnetic Fe_3O_4 NPs, while the larger ones with a size of 16.3 ± 0.9 nm (dark) are Ag NPs.

With a further increase of ε to 13.6 (Fig. 2e), h-NPs were mostly dumbbell-like nanostructures, and the size of the Ag NPs was similar to that obtained at $\varepsilon = 9$, but with a broader size distribution. In addition, the size of Ag NPs in the Fe_3O_4–Ag dumbbell-like structures is similar to that of the Ag NPs (15.0 ± 1.2 nm) synthesised under similar conditions but without Fe_3O_4 seeds (Fig. S3, ESI†). It is clear that the structure and monodispersity of Fe_3O_4–Ag h-NPs depend on the molar ratio of the Ag precursor/Fe_3O_4 seeds in the reaction. The obtained results in our study are consistent with other works where Jian Zhong *et al.*[36] showed core–shell Fe_3O_4@Au h-NPs at a molar ratio of Au precursor to Fe_3O_4 seeds of approximately 7 : 1, while Elvira Fantechi *et al.*[31] obtained dumbbell-like Au–Fe_3O_4 h-NPs at a molar ratio of Fe precursor ($Fe(acac)_3$) to Au seeds of approximately 9.1 : 1. The core@shell structure is confirmed by EDX, elemental mapping and magnetic attraction and Ms measurement in the sections below.

(b) Effect of reaction time. To study the effect of reaction time on the hybrid nanostructures, various syntheses were conducted and the results are listed in Table 1. It can be seen that, at a fixed precursor/seed ratio (ε), the obtained hybrid nano-structure type is almost unchanged but the thickness of the Ag shell (for the core–shell structure) or the size of the Ag NPs (for the dumbbell-like ones) increase with reaction time. The size of core–shell Fe_3O_4@Ag h-NPs (with $\varepsilon = 6.8$) increases from 12.8 nm to 18.5 nm with the reaction time from 30 to 120 min (Fig. S4a1-3, ESI†). The Ag particle size increases from 14.1 nm to 19.2 nm for the reaction times similarly with the dumbbell-like Fe_3O_4–Ag h-NPs (Fig. S4b1-3, ESI†). It is also observed that at shorter reaction times of 30 and 60 min, the obtained h-NPs are uniform (Fig. S4a1-2 and b1-2, ESI†) but then become poly-disperse at a longer reaction time of 120 min (Fig. S4a3 and b3, ESI†). From the above results, a diagram for the formation of the hybrid structure of Fe_3O_4–Ag was suggested and is shown in Fig. 3.

(c) Optical property of Fe_3O_4–Ag h-NPs. The optical properties of some Fe_3O_4–Ag h-NPs were investigated and the results of the UV-vis spectra of Fe_3O_4, pure Ag and Fe_3O_4–Ag h-NPs are shown in Fig. 4a. It can be seen that Fe_3O_4 NPs exhibit no strong absorption peak in the UV-vis spectrum at the wavelength range of 350–800 nm. With the Ag sample, a narrow peak at 405 nm appears on the absorption spectrum due to the typical plasmonic effect of the Ag NPs. For the Fe_3O_4–Ag h-NPs, two SPR peaks at around 410 and 420 nm corresponding to the core–shell and dumbbell-like Fe_3O_4@Ag h-NPs, respectively, were observed in the UV-vis spectra. The dumbbell-like structure has an elevated absorption in the longer wavelength (480–800 nm).

(d) XRD of Fe_3O_4–Ag h-NPs. The structure of Fe_3O_4–Ag h-NPs was confirmed by XRD patterns (Fig. 4b). The XRD results showed that the Fe_3O_4 NPs (seeds) exhibit diffraction peaks at 2-theta values of 30.16, 35.49, 43.01, 53.78, 57.21 and 62.73° corresponding to the reflection planes of (220), (311),

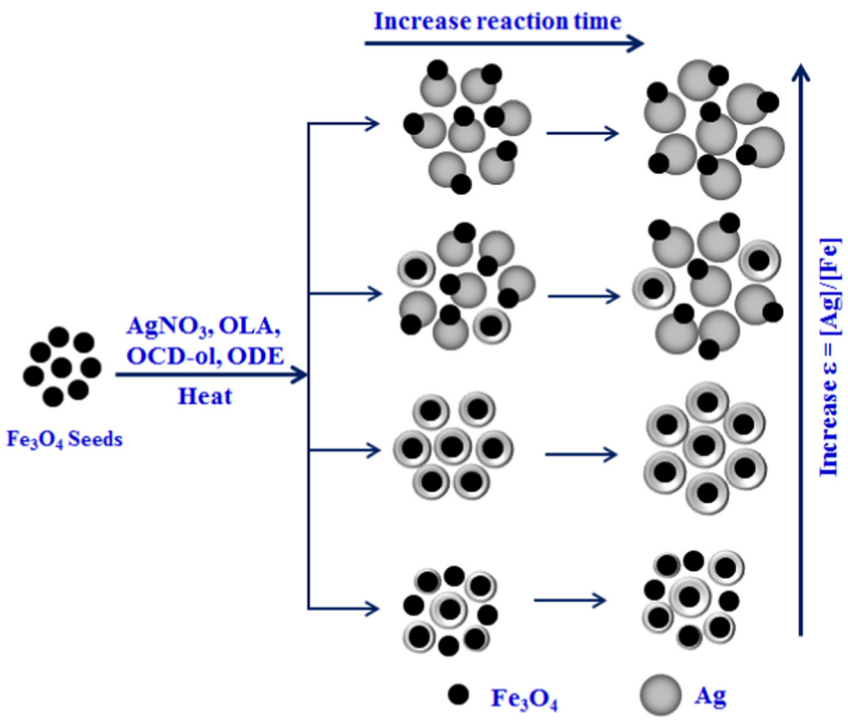

Fig. 3 Schematic diagram of the morphological evolution of Fe_3O_4–Ag h-NPs under different synthetic conditions.

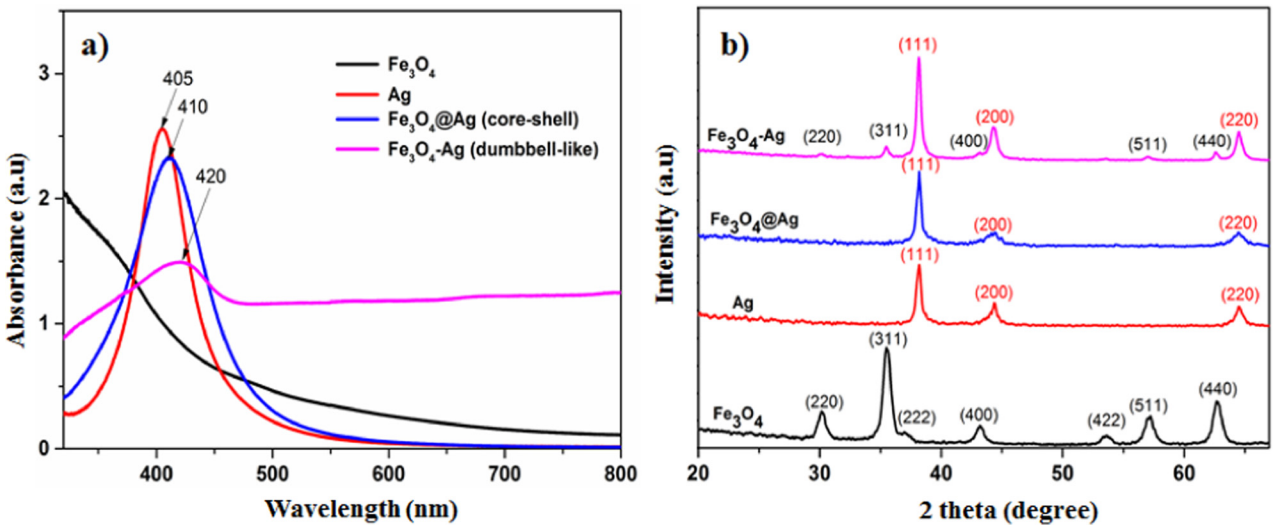

Fig. 4 UV-vis absorption spectra (a) and XRD patterns (b) of Fe_3O_4 NPs (black), Ag NPs (red), core–shell Fe_3O_4@Ag h-NPs (blue) and dumbell-like Fe_3O_4–Ag H-NPs (pink).

(400), (422), (511) and (440) in the inverse-spinel structure of Fe_3O_4 (JCPDS 19-0629). For the core–shell Fe_3O_4@Ag h-NPs, only characteristic peaks at the positions of 38.21, 43.61 and 64.21°, corresponding to the (111), (200) and (220) crystal planes of Ag NPs (JCPDS 004-0783) were observed. The characteristic peaks of Fe_3O_4 NPs were not clearly recorded. This is possible due to the fact that the Fe_3O_4 cores were completely covered by the Ag shell. In addition, the amount of Fe_3O_4 in the core–shell h-NPs is relatively low and so it is hard to detect the presence of the Fe_3O_4 core in core–shell h-NPs using the XRD technique. A similar result was also reported in several works for core–shell h-NPs.[47,48] In the case of dumbbell-like Fe_3O_4–Ag h-NPs, there are typical diffraction peaks for both Ag and Fe_3O_4 NPs. However, the peak intensity of Fe_3O_4 NPs is much lower than that of Ag. The half-width (β) of the typical diffraction peaks of Fe_3O_4 (311) and Ag (111) NPs calculated utilising the Scherrer formula:[49,50]

$$d = \frac{K\lambda}{\beta \cos\theta} \quad (4)$$

where d is the crystallite size of the particles; λ is the wavelength of X-ray radiation; K is a constant, and a K value of 0.89 for spherical shape being used for the calculation.

From the XRD results, the crystallite sizes were calculated being 15.5 nm for core–shell h-NPs, 7.8 nm Fe_3O_4 and 15.7 nm Ag dumbbell-like h-NPs which are in good agreement with those determined from TEM (Fig. 2c and d).

The magnetic properties of the Fe_3O_4 NPs and Fe_3O_4–Ag h-NPs were analysed using vibrating sample magnetometry (VSM) with a magnetic field up to 10 kOe at room temperature. These two samples were superparamagnetic at room temperature to demonstrate the superparamagnetic state of the material sample. The ZFC-FC measurement was performed at a magnetic field of 8 kA m^{-1} with a representative sample of Fe_3O_4 (8.1 nm). As shown in Fig. S5 (ESI†), the ZFC curve has a maximum value of T_B. The T_B temperature is 163.8 K suggesting that the Fe_3O_4 sample is superparamagnetic at room temperature.[51–53]

Fig. 5a shows the magnetisation curves of Fe_3O_4 NPs and Fe_3O_4–Ag h-NPs of some representative samples. It can be seen that all samples reached saturation magnetisation with values of 57.1, 16.5 and 15.1 emu g^{-1} for Fe_3O_4 NPs, core–shell and dumbbell-like Fe_3O_4–Ag h-NPs, respectively. Although the saturation magnetisation value decreases significantly in the Fe_3O_4–Ag h-NPs, they still respond relatively well to the external magnetic field (Fig. 5b). This indicates the magnetic iron oxide component in the hybrid Fe_3O_4–Ag h-NPs. The reduction in the saturation magnetisation value of Fe_3O_4–Ag h-NPs compared with that of Fe_3O_4 NPs is due to the diamagnetic contribution of silver component.[54]

Hollow Fe_3O_4@Au h-NPs

Due to the redox potential difference between metallic pairs, the galvanic replacement reaction is frequently used for the preparation of hollow nanostructures. A void is created by the oxidation of metal crystals which then acts as the template for the formation of the hollow structures. In this work, core–shell Fe_3O_4@Ag h-NPs were used as the nanotemplates for the formation of hollow Fe_3O_4@Au h-NPs through galvanic replacement reaction between Ag and $HAuCl_4$.

Fig. 6 shows TEM images of the hollow Fe_3O_4@Au h-NPs prepared at the volumes of $HAuCl_4$ solution varied in the range of 1.0 to 2.0 mL. It is clear that within the $HAuCl_4$ volume range studied, the hollow nanostructure is formed. At the edge of the hollow structures, the mass contrast is darker than that inside (Fig. 6a–d).

The average perimeter size of the hollow Fe_3O_4@Au h-NPs is around 17 nm, similar to that of the Fe_3O_4@Ag nanotemplates. When the volume of $HAuCl_4$ solution is more than 2.0 mL, the hollow nanostructures are gradually broken (Fig. S6, ESI†).

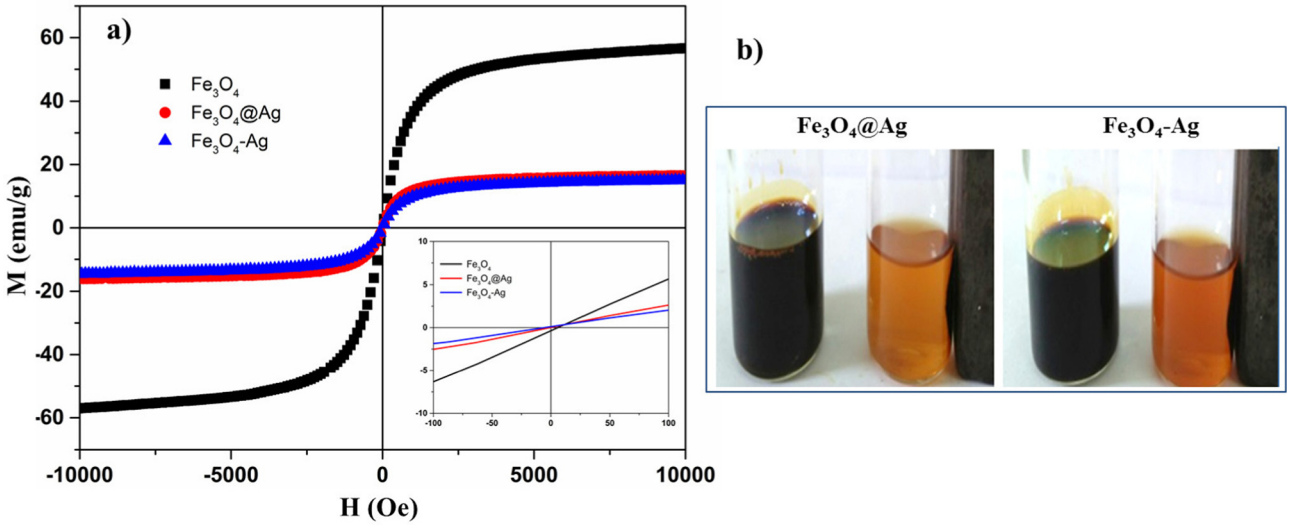

Fig. 5 Magnetization curves of Fe_3O_4 NPs (8.1 nm), core–shell Fe_3O_4@Ag h-NPs (red), dumbbell-like Fe_3O_4–Ag h-NPs (blue) (a) and photographs of h-NPs in *n*-hexane without and with the magnet (b).

At 2.5 mL of $HAuCl_4$ solution, for example, besides the hollow spherical nanoparticles, fragmented NPs are also observed. The hollow nanostructure is completely broken when the volume of the $HAuCl_4$ solution is 3.5 mL (Fig. S6c, ESI†). The dependence of the morphology of the h-NPs on the volumes of $HAuCl_4$ solution used in the synthesis is shown in Table S2 (ESI†).

Fig. 6e shows the magnetisation curves of the Fe_3O_4@Ag nanotemplates and hollow Fe_3O_4@Au h-NPs. The saturation magnetisation value (M_s) of the hollow Fe_3O_4@Au h-NPs is about 20 emu g^{-1}, slightly higher than that of the Fe_3O_4@Ag nanotemplates (16.5 emu g^{-1}) and M_s of the hollow Fe_3O_4@Au samples increases from 17.1 to 22.2 emu g^{-1}, corresponding to the volumes of $HAuCl_4$ solution used from 1.0 to 2.0 mL. This can be explained by the galvanic replacement reaction in which 3 Ag atoms on the Fe_3O_4@Ag nanotemplates were replaced by one Au atom, resulting in the decrease in the weight of the non-magnetic component. The hollow Fe_3O_4@Au h-NPs also exhibit good response to the external magnetic field (Fig. 6e, inset).

Chemical composition of the hollow Fe_3O_4@Au h-NPs was determined through energy dispersive X-ray spectroscopy (EDS) (Fig. S7a and b, ESI†). One can see the characteristic peaks of the main elements, including Fe, Ag and Au. In addition, the low-intensity peaks of C and N were also observed on the EDS spectrum which is due to the contribution of the surfactants. From the elemental mapping analysis, it is obvious that the elements of the hollow Fe_3O_4@Au h-NPs are homogeneously distributed in the sample (Fig. S7c, ESI†).

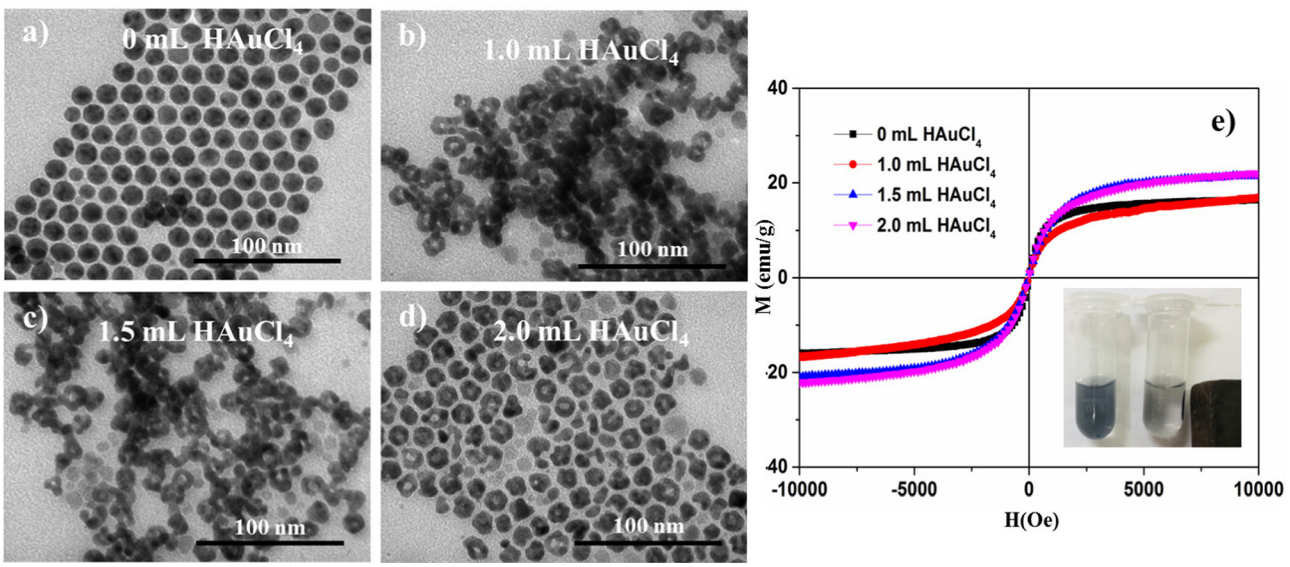

Fig. 6 TEM images of Fe_3O_4@Ag nanotemplates (a) and the hollow Fe_3O_4@Au h-NPs prepared at different $HAuCl_4$ solution volumes: 1.0 (b), 1.5 (c) and 2.0 mL (d), and hysteresis loops (inset: hollow Fe_3O_4@Au h-NPs solution prepared at 2.0 mL $HAuCl_4$ without and with an external magnetic field).

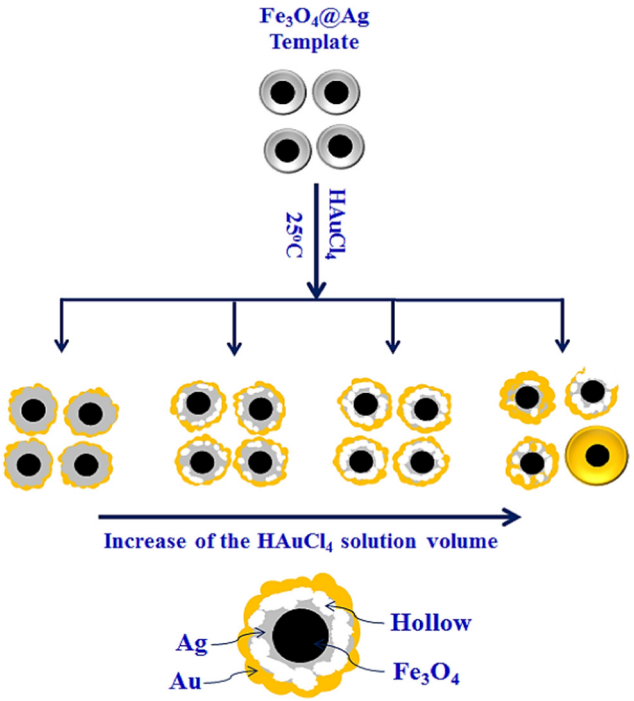

Fig. 7 A schematic illustration of the formation of hollow Fe_3O_4@Au h-NPs with different $HAuCl_4$ amounts.

The influence of the amount of $HAuCl_4$ solution on the formation of the hollow Fe_3O_4@Au h-NPs was originated from the displacement of Ag by Au during galvanic reaction. At the initial stage, Au^{3+} ions are reduced on the surface of Ag (Fe_3O_4@Ag templates) to form an Au shell. Because of the stoichiometry, one Au atom substitutes three Ag atoms, leading to the hollow structure when the amount of $HAuCl_4$ increases.[55] With a further increase in the amount of $HAuCl_4$, the Ag layer disappears, resulting in the collapse of the hollow structure. We propose a schematic diagram of the influence of the amount of $HAuCl_4$ solution on the morphology of hollow Fe_3O_4@Au h-NPs as shown in Fig. 7.

Dispersing hollow Fe_3O_4@Au h-NPs in water

The hydrophobic hollow Fe_3O_4@Au h-NPs were transferred from an organic solvent into an aqueous phase by the encapsulation with PMAO as described in our previous studies.[42,43] The presence of PMAO molecules on the h-NPs surface was determined by Thermogravimetric Analysis (TGA) and Fourier Transform Infrared (FT-IR) measurements. TGA diagrams were recorded under a N_2 atmosphere with a heating rate of 10 °C min^{-1} (Fig. S8a, ESI†). For the sample before phase transfer, OLA coated h-NP (h-NP@OLA), a weight loss of about 10% was observed in the temperature range of 100–450 °C due to the evaporation of water adsorbed on the particle surface and the decomposition of the OLA surfactant. After phase transfer (h-NP@PMAO), a large weight loss of about 58% in the temperature range of 70–600 °C was recorded. This large weight loss is assigned to the loss of water absorption on the particle surface during the storage of the sample (6%), the decomposition of OLA (10%) and PMAO (about 42%).

The presence of PMAO on the surface of h-NPs after phase transfer was also observed through FT-IR measurement (Fig. S8b, ESI†). For the PMAO coated Fe_3O_4@Au h-NPs, a broad band at around 3500 cm^{-1} assigned to the oscillation of the OH group of absorbing water molecules on the PMAO coating was recorded. In both samples, there are peaks at 2853 and 2923 cm^{-1} indicating the presence of CH_2 groups of OLA and PMAO. In the OLA coated Fe_3O_4@Au sample, a peak at 1630 cm^{-1} can be attributed to the amine group of OLA molecules. The presence of PMAO on the surface of h-NPs after phase transfer is confirmed by a strong band at 1570 cm^{-1} assigned to the ionised carboxylic acid groups as the open of the anhydride rings of PMAO molecules under the alkaline environment. These carboxylic groups improve the aqueous dispersion of the PMAO coated h-NPs.

The PMAO coated h-NPs exhibit excellent colloidal stability and dispersibility in water. The dynamic light scattering (DLS) measurement of PMAO coated hollow Fe_3O_4@Au h-NPs (prepared at 2.0 mL $HAuCl_4$ solution) shows only one narrow peak at around 30 nm on the graph, and no aggregation was observed, indicating the colloidal stability (Fig. S9a, ESI†). In addition, the high colloidal stability of the sample was also demonstrated by a high zeta potential value of −40 mV on the surface (Fig. S9b, ESI†).

Fig. 8a shows aqueous solutions of PMAO coated hollow Fe_3O_4@Au h-NPs prepared at the different $HAuCl_4$ contents. By adding different amounts of $HAuCl_4$ solution, the colour of the solution can be changed from yellow (0 mL) to red (0.5 and 1 mL) and cyan (1.5 and 2 mL). Further increasing the amounts of $HAuCl_4$ solution, the solution colour changes from cyan (2 mL) to red (2.5, 3 and 3.5 mL), suggesting the breaking of the hollow Fe_3O_4@Au h-NPs. The colour variations of the solution are also expressed by the strong broad and red-shifting of the SPR absorption bands from 410 to 707 nm when the volume of $HAuCl_4$ solution increases from 0 to 2.0 mL and then the blue-shift to 592, 585 and 565 nm with the increase of the content of $HAuCl_4$ solution to 2.5, 3 and 3.5 mL, respectively (Fig. 8b).

For biomedical applications, materials need to strongly absorb radiation in the near infrared (NIR) region to facilitate deep tissue penetration.[56,57] Therefore, we selected a 2 mL sample of $HAuCl_4$ to carry out further studies.

In vitro cytotoxicity

The cytotoxicity of the h-NPs at various concentrations was evaluated against AGS and MKN45 cell lines using an MTT assay. As seen in Fig. 9a and b, after 24 h of the treatment with the hollow Fe_3O_4@Au h-NPs, the treated cells proliferated significantly faster than the control (untreated) ones. However, when the samples were incubated for 72 h, no significant differences in cell proliferation were found between the two groups. In addition, the morphology of AGS and MKN45 cells developed normally in the treatment conditions after 72 h at 5–40 μg mL^{-1} concentrations of h-NPs (Fig. 9c and d). In both cell lines, nuclei stained with DAPI show a typical morphology of the living cells incubated with the hollow Fe_3O_4@Auh-NPs concentrations of 5–40 μg mL^{-1} (Fig. 9e and f). All of the above

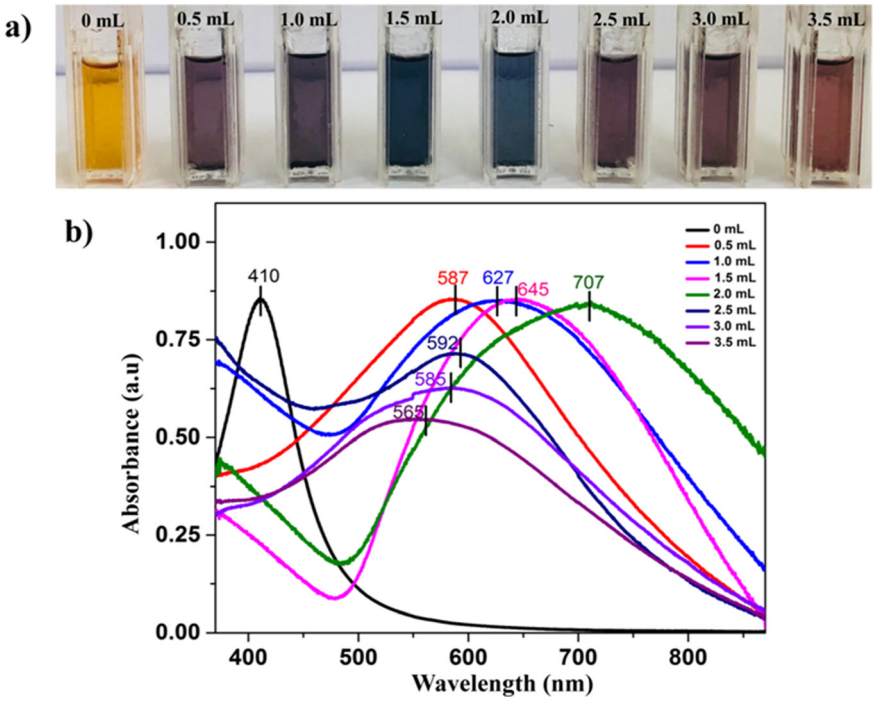

Fig. 8 The color changes (a) and plasmonic absorption spectra (b) of hollow Fe_3O_4@Au h-NPs solution prepared at different $HAuCl_4$ solution volumes from 0 to 3.5 mL.

results show these hollow Fe_3O_4@Au h-NPs affected insignificantly the cellular proliferation, viability and morphology of two gastric cancer cell lines AGS and MKN45 at h-NPs concentrations from 5 to 40 μg mL^{-1}. The obtained result in the current work on the toxicity of Fe_3O_4@Au h-NPs is similar to that of the previous studies.[58,59] For example, Fratoddi and co-workers, in an experiment to evaluate the cytotoxicity of AuNPs to MCF-7 breast cancer cells, indicated that the cell viability of the AuNPs treated sample was higher than that of the control sample (without AuNPs) after 14 days.[60] A similar result was also observed for the prostate cancer cells incubated with Au NPs.[61]

In this work, although the growth of MKN45 and AGS cells treated with h-NPs are higher in the first day of culture, the growth of the h-NP treated cells gradually decreases after 72 h of incubation (Fig. 9). It was well known that NPs are considered an extracellular stimulus as they can bind to EGF-R membrane receptors to trigger cell growth.[62] In our study, the proliferation of the AGS and MKN45 cells treated at low h-NPs concentrations, on the first day of culture with sufficient nutrition, induced proliferation but not apoptosis.

MRI contrast analysis

The most popular MRI sequences are photo shoots with T_1 and T_2 weights. A T_1-weighted image is mainly performed with Gd-based contrast agents (Gads). Gads change the signal strength by shortening T_1 and generating a bright signal on a T_1 weighted image. However, the use of some Gd-chelates in patients with kidney diseases is related to a rare but serious complication called "fibrosis of the kidney system". Meanwhile, magnetic NPs have much larger r_2 transverse recovery, and the dark signal generated by T_2 contrast agents was sometimes confused with some endogenous conditions such as calcification, air, hemorrhage or coagulation. Also with T_2 contrast agent signal reduces with time. Furthermore, the high magnetism of the T_2 contrast agents causes perturbations of the partial magnetic field, which possibly exaggerates the size and dulls the images. Therefore, it's challenging to analyse the MR images, and subsequently, in practical application (clinical diagnosis) the negative contrast agents are rarely used.

In the current study, the contrast effects of the hollow Fe_3O_4@Au h-NPs were evaluated by measuring the MRI signals at different h-NPs concentrations and compared with those of the conventional contrast agents (Table S3, ESI†). In addition, the influence of scan parameters on the MR relaxations was also investigated. Fig. 10 and 11 show the dependence of MR relaxations on the h-NPs concentrations and the scan parameters. The contrast is seen to change by varying a small value of the particle concentration. It was well known that, on the spin-echo (SE) image, the repetition time (TR) and the time to echo (TE) were used to control the image contrast and the weighting of the MR image. The overall signal strength (S) of the SE sequence can be determined by the expression:

$$S = K\cdot[H]\cdot(1 - e^{-TR/T_1})\cdot e^{-TE/T_2} \quad (5)$$

where $[H]$ is the spin (proton) density and K is a scaling factor.

When TE is shorter than T_2, the ratio $TE/T_2 \rightarrow 0$, so the T_2 weight term $e^{-TE/T_2} \rightarrow 1$. In other words, the T_2 effect rapidly disappears. In contrast, as TE is longer than T_2, the importance of the weight condition exponentially increases. In other words,

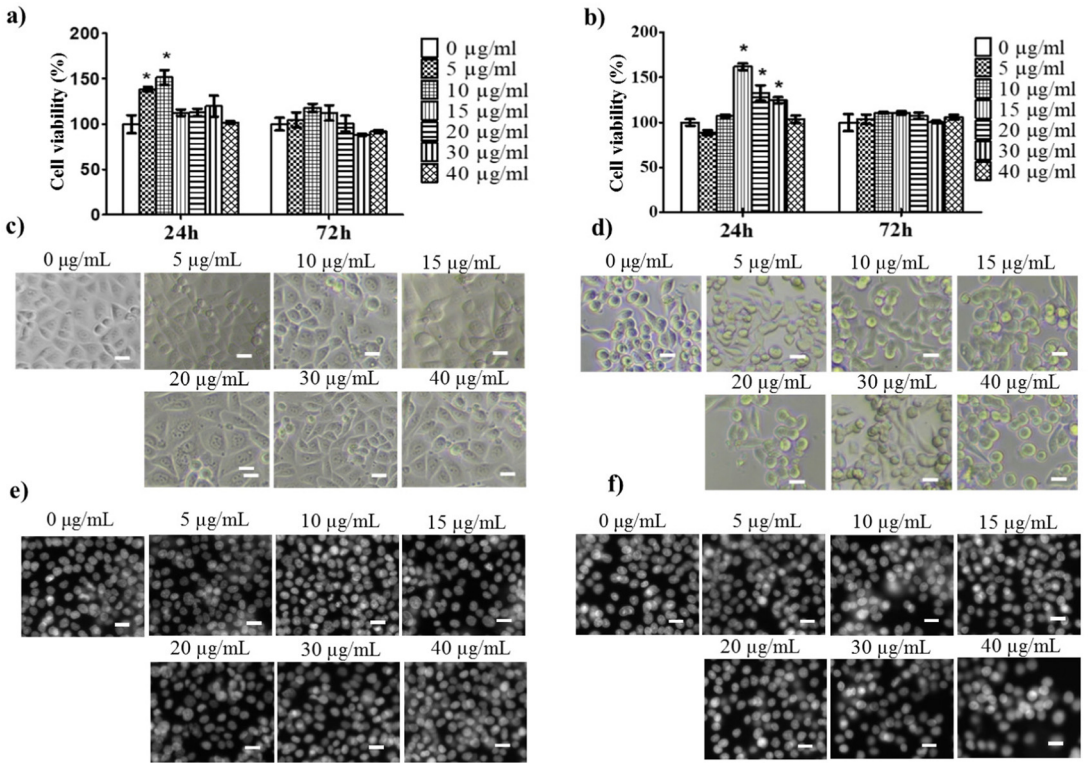

Fig. 9 The influence of the hollow Fe_3O_4@Au h-NPs on cellular proliferation, cellular and nuclear morphology of gastric cancer cell lines of AGS and MKN45. AGS (a) and MKN45 (b) cells were treated with Fe_3O_4@Au h-NPs at different concentrations of 5–40 μg mL^{-1} after 24 and 72 h of treatment; Representative images of cellular morphology of AGS (c) and MKN45 (d) cells and nuclear morphology of AGS (e) and MKN45 (f) cells treated or untreated with the hollow Fe_3O_4@Au h-NPs for 72 h. Cell viability was determined by MTT assays (n = 5). *$P \leq 0.05$ compared with the control; Mann-Whitney test. Scale bar: 50 μm.

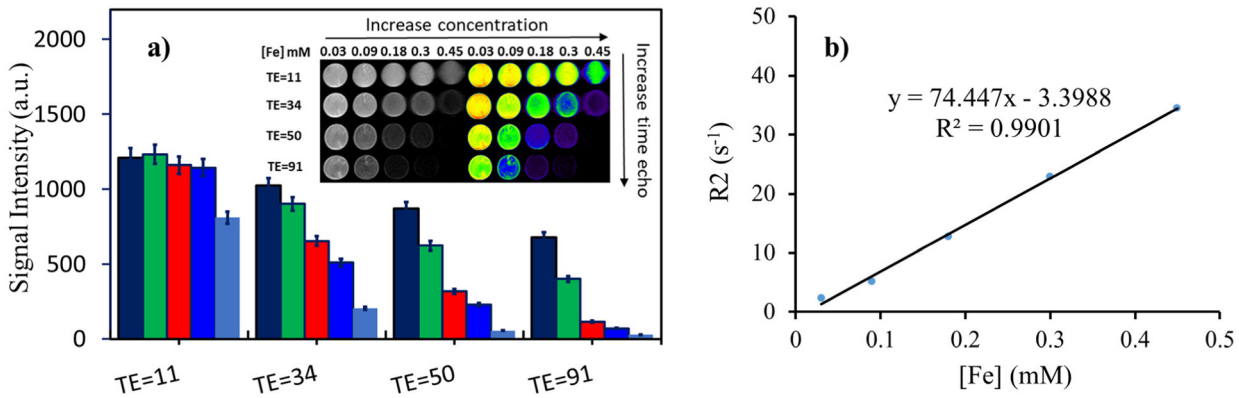

Fig. 10 T_2 weighted MR image and signal intensity of the hollow Fe_3O_4@Au h-NPs at the different Fe concentrations of 0.03 (dark blue), 0.09 (green), 0.18 (red), 0.3 (blue) and 0.45 mM (light blue) and echo times of 11, 34, 50 and 91 ms (a) and the linear fitting of $1/T_2$ *versus* the Fe concentrations (b). TR was fixed at 4000 ms.

the effect of TE on T_2 weight is considered based on the signals produced by two tissues with different T_2 values. When TE is short, echo occurs when there is little time to decay T_2 and thus the tissues are not differentiated. If TE is long, the relative difference in signal decomposition between two or more tissues becomes more noticeable, and thus there are more "T_2-weighted".

Similar arguments can be made for the interaction between TR and T_1. When TR is longer than T_1, the term has T_1 e^{-TR/T_1} → 0 term, so the T_1 effect disappears. Over the long term, all tissues of TR with different T_1 values require time to recover from a 90° excitation pulse, so their signals are not significantly different. In contrast, a short TR highlights "T_1-weighted".

In clinical practice, TE is always much shorter than TR, with values as low as possible, and usually less than 30 ms for T_1-weighted images. Meanwhile, for T_2-weighted images, TR and TE must be long, typically greater than 2500 ms and 90 ms,

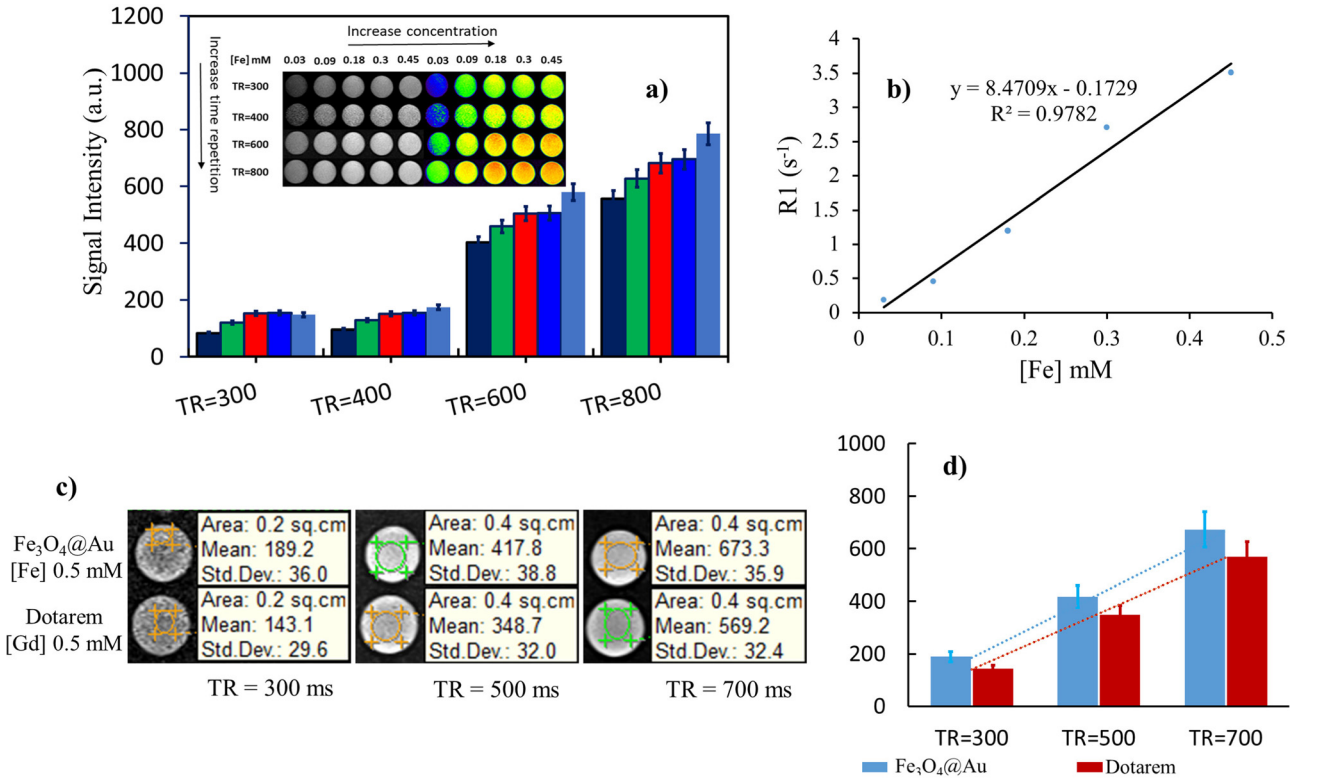

Fig. 11 T_1 weighted MR images and signal intensity of the hollow Fe_3O_4@Au h-NPs at various Fe concentrations of 0.03 (dark blue), 0.09 (green), 0.018 (red), 0.3 (blue) and 0.45 mM (light blue) and repetition times TR of 300, 400, 600 and 800 ms (a) and the linear fitting of $1/T_1$ against the Fe concentrations (b); T_1-weighted MRI images (c) and the intensity (d) of the hollow Fe_3O_4@Au h-NPs and Dotarem at different TR values (300, 500 and 700 ms). Echo time TE was fixed at 11 ms.

respectively. MRI data shown in Fig. 10a indicate that TE in the T_2-weighted image with a value of 91 ms gives a much lower signal intensity than the TE values of 50, 34 and 11 ms. In addition, the signal intensity also decreases with the increase of the concentration of the hollow Fe_3O_4@Au h-NPs. This means that the T_2-weighted image is darker at longer echo times TE and higher particle concentrations. For T_1-weighted images, both TR and TE are significantly shorter than for T_2-weighted ones but the longer TR values give the stronger signal strength (Fig. 11a). In comparison with Dotarem, a Gd-based, commercial and clinical contrast agent, the hollow Fe_3O_4@Au h-NPs exhibit a signal strength increase of about 20 to 34% at the different TR values (Fig. 11c and d). In clinical use, bright signals produced by T_1 contrast agents are usually preferred for better clarity than the dark signals produced by T_2 contrast agents which are sometimes confusing in some endogenous conditions, such as calcification, air, hemorrhage or blood clots.

As shown in Fig. 10 and 11, the hollow Fe_3O_4@Au h-NPs exhibit relatively high r_1 and r_2 values of 8.47 and 74.45 mM^{-1} s^{-1}, respectively. It was also well known that the ratio of r_2/r_1 is also an important parameter to evaluate the efficiency of T_1 and T_2 contrast agents. The higher the r_2/r_1 ratio, the T_2 mode image is dominant while the T_1 mode image can be achieved at a lower r_2/r_1 ratio. It was indicated that MRI contrast agents with a large r_2/r_1 ratio (>10) can be used as T_2 contrast agents and the ones with a small r_2/r_1 ratio (<5) are usually used as T_1 contrast agents and the ones with r_2/r_1 ratio values between 5 and 10 are used as T_1–T_2 dual-mode MRI contrast agents.[63,64]

In the current study, the ratio of r_2/r_1 of the hollow Fe_3O_4@Au h-NPs is 8.79, which is significantly higher than those of most commercial contrast agents, for example, Dotarem (1.19), Magnevist (1.12), MultiHance (1.38) or Gadovist (1.17) (Table S3, ESI†). The r_2/r_1 value of the h-NPs is lower than that of SPION-based T_2 contrast agents, including Ferumoxtran, Resovist® or Feridex® (Table S3, ESI†). Due to the high r_1 relaxivity of 8.47 mM^{-1} s^{-1}, the h-NPs have potential to be applied as an effective T_1 contrast agent. In addition, the high r_2/r_1 ratio of the h-NPs suggests that the h-NPs can be used as both T_1 and T_2 contrast agents. To evaluate the h-NPs as T_1 positive and T_2 negative contrast agents, the calculated values of r_1 and r_2 of the Fe_3O_4@Au h-NPs were compared with those of other types of MRI contrast agents (Table S3, ESI†).

Magnetic and photo induced heating of the hollow Fe_3O_4@Au h-NPs

To assess the heat generation of the hollow Fe_3O_4@Au h-NPs, three heating modes were carried out. The experimental model is depicted as shown in Fig. S10 (ESI†). First, the MIH of the h-NPs was examined by subjecting the h-NP fluids to an alternating magnetic field at an applied field of 16 kA m^{-1} and a frequency of 450 kHz. Second, the h-NP fluids were

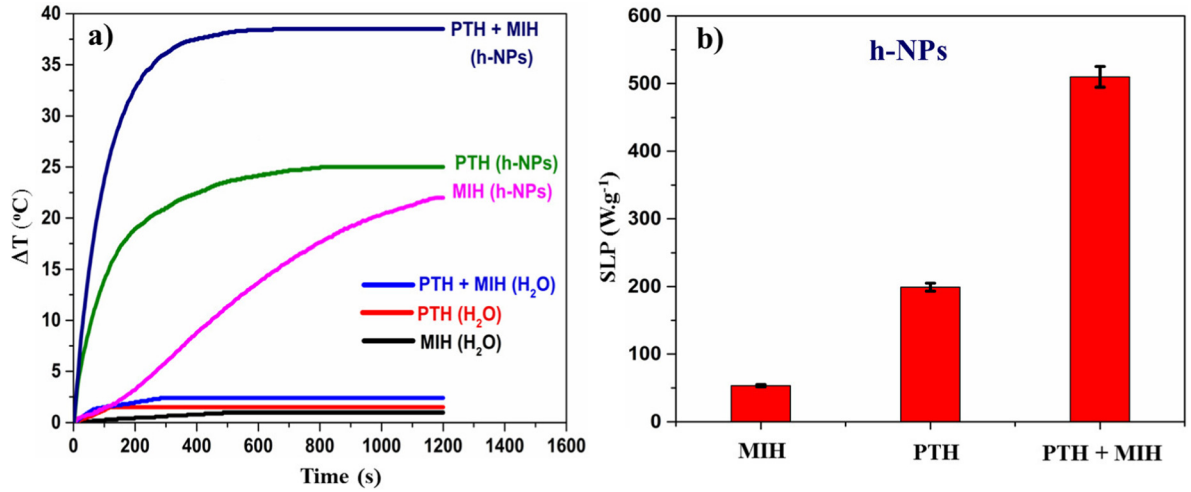

Fig. 12 The heating curves for the hollow Fe_3O_4@Au h-NPs solutions and H_2O (a), and the corresponding SLP values of the h-NPs solutions obtained under different conditions: an applied field of 16 kA m^{-1} at a frequency 450 kHz and a laser power density 0.65 W cm^{-2} (b).

irradiated with an 808 nm diode laser at a density power of 0.65 W cm^{-2} to assess the photo-generated heat (PTH) and finally, both modes of MIH and PTH were applied simultaneously (*i.e.* the dual heating). All the measurements were made at a concentration of the aqueous h-NPs fluid of 3 mg mL^{-1}. Fig. 12 shows the time-dependent temperature increase of the h-NPs fluids under the three heating modes and the SLP value corresponding to the heating curve of the h-NPs solution. It is clear that the rate of temperature increased by the dual heating was considerably higher than those of the two other single modes. With the simultaneous irradiation of MIH and PTH, the increase of temperature was 38.5 °C, significantly larger than that in the cases of PTH (25.0 °C) or MIH (22.0 °C) (Fig. 12a). Pure water as the control showed a very low temperature increment (1.0–2.5 °C) under all three modes, indicating that the temperature increase of the samples was due to the heating effect of the hollow Fe_3O_4@Au h-NPs. The negligible temperature increase in the control sample was caused by the weak influence of the magnetic field and absorption laser light of water.

The calculated maximum SLP value of the hollow Fe_3O_4@Au h-NP fluids was 510 W g^{-1} for simultaneous heating (PTH + MIH) (Fig. 12b). It is about 2.6 and 9.6 times greater than that of the single PTH (199.1 W g^{-1}) and MIH (53.2 W g^{-1}), respectively. The temperature increase for dual heating of Fe_3O_4@Au fluids is quantitatively comparable with the results reported by Ana Espinosa *et al.* where the temperature increments of Fe_3O_4 nanocubes at a 5 mg Fe mL^{-1} concentration subjected to PTH (1 W cm^{-2}) and MIH (470 kHz and 14.32 kA m^{-1}).[65] Fan Yang *et al.* reported the temperature increase of 31 °C for Fe_3O_4-PbS/CdS hybrid nanomaterials under the combined magnetic/photo heating (with 10 mM h-NPs, the intensity of laser at 3.3 W cm^{-2}, the magnetic field of 150 kHz and 7 kA m^{-1}.[66] In our work, the combination of MIH and PTH was within the safe application range (with a magnetic field of 16 kA m^{-1} and a frequency of 450 kHz, and 808 nm NIR laser at a power density of 0.65 W cm^{-2}).

The heating efficiency of the hollow Fe_3O_4@Au h-NPs by the combined modes of the magnetic field and the laser at different intensities was also investigated. Fig. S11a (ESI†) shows the heating curves of the hollow Fe_3O_4@Au h-NPs solutions under different applied fields of 8–20 kA m^{-1}, at a constant frequency of 450 kHz and an 808 nm laser with a power density of 0.5 W cm^{-2}. The results show the dependence of temperature on the intensity of the external magnetic field. When the magnetic field strength increases from 8 to 20 kA m^{-1}, the sample temperature variation increases from 17 to 38 °C. The temperature increased very rapidly during the first 300 s of the treatment, then the increase slowed down and reached saturation after 1200 s. The results in Fig. S11b (ESI†) show that the SLP values changed when applying magnetic fields at different intensities. A maximum value of SLP ~ 350 W g^{-1} is reached at an applied magnetic field of 20 kA m^{-1}, a frequency 450 kHz and a laser power density of 0.5 W cm^{-2}.

The heating efficiency of the hollow Fe_3O_4@Au h-NPs under a constant applied field of 16 kA m^{-1} at a frequency of 450 kHz and different power densities is shown in Fig. S11c and d (ESI†). It can be seen that the temperature of the aqueous solution containing the hollow Fe_3O_4@Au h-NPs increased with the increasing irradiation time at the laser power density of 0.2–0.65 W cm^{-2}. The sample temperature variation increased from 16 to 38.5 °C for a laser power density varied from 0.2 to 0.65 W cm^{-2}. The results in Fig. S11d (ESI†) show that the SLP value changes (125.3–510 W g^{-1}) under an irradiation laser at different power densities. It also shows a high optical/magnetic-thermal conversion efficiency and thermal stability during the exposure to the combined laser and magnetic field. This variation trend is similar to the hollow Au NPs, which were investigated at a laser power density of 0.35–1.6 W cm^{-2} in our previous study.[42] However, the heating efficiency corresponding to the simultaneous heating (PTH and MIH) of the hollow Fe_3O_4@Au h-NPs is significantly larger than that of PTH for the hollow Au NPs. Therefore, the combination of magnetic fields and laser

exposure of the hollow Fe_3O_4@Au h-NPs is a promising method for cancer treatment.

In addition, the influence of the hollow Fe_3O_4@Au h-NPs concentration on the heating efficiency was investigated. Fig. S12 (ESI†) presented the heating curves and the corresponding SLP values of the hollow Fe_3O_4@Au h-NPs solutions at the concentrations of 1, 2, and 3 mg mL^{-1}. It can be seen that the solution temperature variation increases from 18.1 to 38.5 °C with the increase of sample concentration from 1 to 3 mg mL^{-1}, respectively (Fig. S12a, ESI†). Based on their heating curves, the SLP values were 672.2, 593.5, and 510 W g^{-1} at the concentrations of 1, 2, and 3 mg mL^{-1}, respectively (Fig. S12b, ESI†). The decrease of the SLP value with the increase of the concentration of the hollow Fe_3O_4@Au h-NPs in magnetic fluids was possible due to the increase in dipole interaction at a high sample concentration which was previously observed.[67,68]

Conclusions

The hollow Fe_3O_4@Au h-NPs with an average size of around 17 nm were successfully prepared. Due to the gap formed between the Fe_3O_4 core and the Au shell, Fe_3O_4@Au h-NPs exhibit strong absorption in the NIR region. The hollow Fe_3O_4@Au h-NPs were transferred into water by the encapsulation with an amphiphilic PMAO polymer to form a high colloidally stable solution. The results of the toxicity tests indicate that hollow Fe_3O_4@Au h-NPs affect insignificantly the proliferation, viability and morphology of two gastric cancer cell lines of AGS and MKN45 at various concentrations from 5 to 40 μg mL^{-1}. The MR data show that PMAO encapsulated hollow Fe_3O_4@Au h-NPs are powerful dual-modal imaging contrast agents for T_1 and T_2 MRI (r_1 = 8.47 mM^{-1} s^{-1}, r_2 = 74.45 mM^{-1} s^{-1}). In addition, the magnetic and photothermal data of h-NPs indicate that sample temperature can reach 70 °C under a relatively low laser power and a magnetic field intensity of 0.65 W cm^{-2} and 16 kA m^{-1}, respectively, showing effective combination between the magnetic thermal potential of iron oxide cores and the photothermal effects of the gold shell into an efficient dual modal thermo-therapy. Our study demonstrates the potential of using hollow Fe_3O_4@Au h-NPs for T_1–T_2 dual mode MRI and dual magnetic and photothermal therapy.

Author contributions

Nguyen T. N. Linh, Ngo T. Dung, Le T. T. Tam: synthesis of materials; Le T. T. Tam: performed measurements (XRD, TEM, UV-vis, EDS); Le T. Tam, Pham. H. Nam, Nguyen V. Dang, Le D. Tung: performed analysis and assessment of morphology and structure, magnetic properties analysis, structural characterization analysis, and carried out and analysis magnetic/optical heating; Le V. Thanh, Nguyen V. Dong, Le G. Nam, Le T. Tam: MR imaging analysis Nguyen D. Vinh, Nguyen P. Hung, Ngo T. Ha: *In vitro* cytotoxicity assay; Nguyen T. N Linh: writing – original draft; Nguyen X. Phuc, Le D. Tung, Nguyen T. K. Thanh and Le T. Lu: supervision, writing – review & editing. All authors read and approved the final manuscript.

Conflicts of interest

There are no conflicts to declare.

Acknowledgements

This research is funded by the Vietnam National Foundation for Science and Technology Development (NAFOSTED) under grant number 103.02-2017.334.

References

1 L. Carbone and P. D. Cozzoli, *Nano Today*, 2010, **5**, 449.
2 C. de Mello Donega, *Chem. Soc. Rev.*, 2011, **40**, 1512–1546.
3 R. D. Corato, G. Béalle, J. Kolosnjaj-Tabi, A. Espinosa, O. Clément, A. K. A. Silva, C. Ménager and C. Wilhelm, *ACS Nano*, 2015, **9**, 2904–2916.
4 Y. Mao, P. Yi, Z. Deng and J. Ge, *CrystEngComm*, 2013, **15**, 3575–3581.
5 W. Wu, T. Zhou, A. Berliner, P. Banerjee and S. Zhou, *Chem. Mater.*, 2010, **22**, 1966–1976.
6 J. Kim, Y. Piao and T. Hyeon, *Chem. Soc. Rev.*, 2009, **38**, 372–390.
7 Y. Lu, C. Shi, M. J. Hu, Y. J. Xu, L. Yu, L. P. Wen, Y. Zhao, W. P. Xu and S. H. Yu, *Adv. Funct. Mater.*, 2010, **20**, 3701–3706.
8 A. Riedinger, M. P. Leal, S. R. Deka, C. George, I. R. Franchini, A. Falqui, R. Cingolani and T. Pellegrino, *Nano Lett.*, 2011, **11**, 3136–3141.
9 Z. Nemati, J. Alonso, H. Khurshid, M. H. Phan and H. Srikanth, *RSC Adv.*, 2016, **6**, 38697–38702.
10 K. C.-F. Leung, S. Xuan, X. Zhu, D. Wang, C.-P. Chak, S.-F. Lee, W. K.-W. Hob and B. C.-T. Chungb, *Chem. Soc. Rev.*, 2012, **41**, 1911–1928.
11 C. Wang, C. Xu, H. Zeng and S. Sun, *Adv. Mater.*, 2009, **21**, 3045–3052.
12 H. Kakwere, M. E. Materia, A. Curcio, M. Prato, A. Sathya, S. Nittia and T. Pellegrino, *Nanoscale*, 2018, **10**, 3930–3944.
13 S. Liu, S. Guo, S. Sun and X. Z. You, *Nanoscale*, 2015, **7**, 4890–4893.
14 C. Wang, H. Yin, S. Dai and S. Sun, *Chem. Mater.*, 2010, **22**, 3277–3282.
15 C. George, A. Genovese, A. Casu, M. Prato, M. Povia, L. Manna and T. Montanari, *Nano Lett.*, 2013, **13**, 752–757.
16 S. Najafishirtari, P. Guardia, A. Scarpellini, M. Prato, S. Marras, L. Manna and M. Colombo, *J. Catal.*, 2016, **338**, 115–123.
17 J. Huang, Y. Cao, Q. Shao, X. Peng and Z. Guo, *Ind. Eng. Chem. Res.*, 2017, **56**, 10689–10701.
18 K. Gong, Q. Hu, L. Yao, M. Li, D. Sun, Q. Shao, B. Qiu and Z. Guo, *ACS Sustainable Chem. Eng.*, 2018, **6**, 7283–7291.

19 H. Wang, J. Shen, G. Cao, Z. Gai, K. Hong, P. R. Debata, P. Banerjee and S. Zhou, *J. Mater. Chem. B*, 2013, **1**, 6225–6234.
20 B. Chudasama, A. K. Vala, N. Andhariya, R. V. Upadhyay and R. V. Mehta, *J. Magn. Magn. Mater.*, 2011, **323**, 1233–1237.
21 A. Amarjargal, L. D. Tijing, I. T. Im and C. S. Kim, *Chem. Eng. J.*, 2013, **226**, 243–254.
22 M. E. F. Brollo, J. M. Orozco-Henao, R. López-Ruiz, D. Muraca, C. S. B. Dias, K. R. Pirota and M. Knobel, *J. Magn. Magn. Mater.*, 2016, **397**, 20–27.
23 Q. Ding, D. Liu, D. Guo, F. Yang, X. Pang, R. Che, N. Zhou, J. Xie, J. Sun, Z. Huang and N. Gu, *Biomaterials*, 2017, **124**, 35–46.
24 C. Multari, M. Miola, F. Laviano, R. Gerbaldo, G. Pezzotti, D. Debellis and E. Verné, *Nanotechnology*, 2019, **30**, 255705–255727.
25 Q. Lu, X. Dai, P. Zhang, X. Tan, Y. Zhong, C. Yao, M. Song, G. Song, Z. Zhang, G. Peng, Z. Guo, Y. Ge, K. Zhang and Y. Li, *Int. J. Nanomed.*, 2018, **13**, 2491–2505.
26 A. Espinosa, M. Bugnet, G. Radtke, S. Neveu, G. A. Botton, C. Wilhelm and A. Abou-Hassan, *Nanoscale*, 2015, **7**, 18872–18877.
27 S. K. Sharma, N. Shrivastava, F. Rossi, L. D. Tung and N. T. K. Thanh, *Nano Today*, 2019, **29**, 100795–100821.
28 Y. Wei, R. Klajn, A. O. Pinchuk and B. A. Grzybowski, *Small*, 2008, **4**, 1635–1639.
29 H. Zeng and S. Sun, *Adv. Funct. Mater.*, 2008, **18**, 391–400.
30 M. Felber and R. Alberto, *Nanoscale*, 2015, **7**, 6653–6660.
31 E. Fantechi, A. G. Roca, B. Sepúlveda, P. Torruella, S. Estradé, F. Peiró, E. Coy, S. Jurga, N. G. Bastús, J. Nogués and V. Puntes, *Chem. Mater.*, 2017, **29**, 4022–4035.
32 M. Abbas, S. RamuluTorati and C. G. Kim, *Dalton Trans.*, 2017, **46**, 2303–2309.
33 S. Rajkumar and M. Prabaharan, *Colloids Surf., B*, 2019, **174**, 252–259.
34 D. Kim, M. K. Yu, T. S. Lee, J. J. Park, Y. Y. Jeong and S. Jon, *Nanotechnology*, 2011, **22**, 155101–155107.
35 Z. Xu, Y. Hou and S. Sun, *J. Am. Chem. Soc.*, 2007, **129**, 8698–8699.
36 W. Wang, J. Luo, Q. Fan, M. Suzuki, I. S. Suzuki, M. H. Engelhard, Y. Lin, N. Kim, J. Q. Wang and C.-J. Zhong, *J. Phys. Chem. B*, 2005, **109**, 21593–21601.
37 Y. Jin, C. Jia, S. W. Huang, M. O'Donnell and X. Gao, *Nat. Commun.*, 2010, **1**, 1–8.
38 L. S. Lin, X. Yang, Z. Zhou, Z. Yang, O. Jacobson, Y. Liu, A. Yang, G. Niu, J. Song, H.-H. Yang and X. Chen, *Adv. Mater.*, 2017, **29**, 1606681–1606689.
39 J. Zeng, M. Gong, D. Wang, M. Li, W. Xu, Z. Li, S. Li, D. Zhang, Z. Yan and Y. Yin, *Nano Lett.*, 2019, **19**, 3011–3018.
40 E. C. Dreaden, A. M. Alkilany, X. Huang, C. J. Murphy and M. A. El-Sayed, *Chem. Soc. Rev.*, 2012, **41**, 2740–2779.
41 L. T. Lu, N. T. Dung, L. D. Tung, C. T. Thanh, O. K. Quy, N. V. Chuc, S. Maenosono and N. T. K. Thanh, *Nanoscale*, 2015, **7**, 19596–19610.
42 N. T. Dung, N. T. N. Linh, D. L. Chi, N. T. H. Hoa, N. P. Hung, N. T. Ha, P. H. Nam, N. X. Phuc, L. T. Tam and L. T. Lu, *RSC Adv.*, 2021, **11**, 13458–13465.
43 N. T. Dung, N. V. Long, L. T. T. Tam, P. H. Nam, L. D. Tung, N. X. Phuc, L. T. Lu and N. T. K. Thanh, *Nanoscale*, 2017, **9**, 8952–8961.
44 P. H. Nam, N. X. Phuc, P. H. Linh, L. T. Lu, D. H. Manh, P. T. Phong and I.-J. Lee, *Phys. B*, 2018, **550**, 428–435.
45 T. K. O. Vuong, D. L. Tran, T. L. Le, D. V. Pham, H. N. Pham, T. H. L. Ngo, H. M. Do and X. P. Nguyen, *Mater. Chem. Phys.*, 2015, **163**, 537–544.
46 S. G. Kwon, G. Krylova, P. J. Phillips, R. F. Klie, S. Chattopadhyay, T. Shibata, E. E. Bunel, Y. Liu, V. B. Prakapenka, B. Lee and E. V. Shevchenko, *Nat. Mater.*, 2014, **14**, 215–223.
47 M. Mandal, S. Kundu, S. K. Ghosh, S. Panigrahi, T. K. Sau, S. M. Yusuf and T. Pal, *J. Colloid Interface Sci.*, 2005, **286**, 187–194.
48 J. C. Park, G. T. Lee and J. H. Seo, *J. Mater. Sci.*, 2017, **52**, 1534–1545.
49 H. P. Klug and L. E. Alexander, *J. Am. Chem. Soc.*, 2005, **77**, 2030–2031.
50 H. Borchert, E. V. Shevchenko, A. Robert, I. Mekis, A. Kornowski, G. Grübel and H. Weller, *Langmuir*, 2005, **21**, 1931–1936.
51 M. Jeun, S. Lee, J. K. Kang, A. Tomitaka, K. W. Kang, Y. Il Kim, Y. Takemura, K. W. Chung, J. Kwak and S. Bae, *Appl. Phys. Lett.*, 2012, **100**, 092406–092409.
52 K. Koch, M. Kundt, A. Barkane, H. Nadasi, S. Webers, J. Landers, H. Wende, A. Eremin and A. M. Schmidt, *Phys. Chem. Chem. Phys.*, 2021, **23**, 24557–24569.
53 D. Sarkar and M. Mandal, *J. Phys. Chem. C*, 2012, **116**, 3227–3234.
54 G. Jiang, Y. Huang, S. Zhang, H. Zhu, Z. Wu and S. Sun, *Nanoscale*, 2016, **8**, 17947–17952.
55 S. V. Jenkins, T. D. Gohman, E. K. Miller and J. Chen, *J. Chem. Educ.*, 2015, **92**, 1056–1060.
56 D. Jaque, L. M. Maestro, B. del Rosal, P. H. Gonzalez, A. Benayas, J. L. Plaza, E. M. Rodríguez and J. G. Solé, *Nanoscale*, 2014, **6**, 9494–9530.
57 J. Zeng, M. Gong, D. Wang, M. Li, W. Xu, Z. Li, S. Li, D. Zhang, Z. Yan and Y. Yin, *Nano Lett.*, 2019, **19**, 3011–3018.
58 C. Hoskins, Y. Min, M. Gueorguieva, C. McDougall, A. Volovick, P. Prentice, Z. Wang, A. Melzer, A. Cuschieri and L. Wang, *J. Nanobiotechnol.*, 2012, **10**, 1.
59 G. Wang, W. Gao, X. Zhang and X. Mei, *Sci. Rep.*, 2016, **6**, 28258–28267.
60 I. Fratoddi, I. Venditti, C. Cametti and M. V. Russo, *J. Mater. Chem. B*, 2014, **2**, 4204–4220.
61 W. Roa, X. Zhang, L. Guo, A. Shaw, X. Hu, Y. Xiong, S. Gulavita, S. Patel, X. Sun and J. Chen, *Nanotechnology*, 2009, **20**, 375101–375109.
62 U. Sydlik, K. Bierhals, M. Soufi, J. Abel, R. P. F. Schins and K. Unfried, *Am. J. Physiol. - Lung Cell. Mol. Physiol.*, 2006, **291**, 725–734.
63 Y. K. Peng, S. C. E. Tsang and P. T. Chou, *Mater. Today*, 2015, **19**, 336–348.
64 W. Zhang, L. Liu, H. Chen, K. Hu, I. Delahunty, S. Gao and J. Xie, *Theranostics*, 2018, **8**, 2521–2548.

65 A. Espinosa, K.-T. Jelena, A.-H. Ali, A. P. Sangnier, A. Curcio, A. K. A. Silva, R. Di Corato, S. Neveu, T. Pellegrino, L. M. Liz-Marzán and C. Wilhelm, *Adv. Funct. Mater.*, 2018, **28**, 1803660.
66 F. Yang, A. Skripka, M. S. Tabatabaei, S. H. Hong, F. Ren, A. Benayas, J. K. Oh, S. Martel, X. Liu, F. Vetrone and D. Ma, *ACS Nano*, 2019, **13**, 408–420.
67 V. M. Khot, A. B. Salunkhe, N. D. Thorat, M. R. Phadatare and S. H. Pawar, *J. Magn. Magn. Mater.*, 2013, **332**, 48–51.
68 P. H. Linh, N. X. Phuc, L. V. Hong, L. L. Uyen, N. V. Chien, P. H. Nam, N. T. Quy, H. T. M. Nhung, P. T. Phong and I.-J. Lee, *J. Magn. Magn. Mater.*, 2018, **460**, 128–136.